ACS Catalysis
Research Article
pubs.acs.org/acscatalysis

Role of the Support and Reaction Conditions on the Vapor-Phase Deoxygenation of *m*-Cresol over Pt/C and Pt/TiO_2 Catalysts

Michael B. Griffin,[†] Glen A. Ferguson,[†] Daniel A. Ruddy, Mary J. Biddy, Gregg T. Beckham,* and Joshua A. Schaidle*

National Bioenergy Center, National Renewable Energy Laboratory, 15013 Denver West Parkway, Golden, Colorado 80401, United States

Ⓢ *Supporting Information*

ABSTRACT: The catalytic deoxygenation of biomass fast pyrolysis vapors offers a promising route for the sustainable production of liquid transportation fuels. However, a clear understanding of the mechanistic details involved in this process has yet to be achieved, and questions remain regarding the role of the catalyst support and the influence of reaction conditions. In order to gain insight into these questions, the deoxygenation of *m*-cresol was investigated over Pt/C and Pt/TiO_2 catalysts using experimental and computational techniques. The performance of each catalyst was evaluated in a packed-bed reactor under two conditions (523 K, 2.0 MPa and 623 K, 0.5 MPa), and the energetics of the ring hydrogenation, direct deoxygenation, and tautomerization mechanisms were calculated over hydrogen-covered Pt(111) and oxygen vacancies on the surface of TiO_2(101). Over Pt(111), ring hydrogenation to 3-methylcyclohexanone and 3-methylcyclohexanol was found to be the most energetically favorable pathway. Over TiO_2(101), tautomerization and direct deoxygenation to toluene were identified as additional energetically favorable routes. These calculations are consistent with the experimental data, in which Pt/TiO_2 was more active on a metal site basis and exhibited higher selectivity to toluene at 623 K relative to Pt/C. On the basis of these results, it is likely that the reactivity of Pt/TiO_2 and Pt/C is driven by the metallic phase at 523 K, while contributions from the TiO_2 support enhance deoxygenation at 623 K. These results highlight the synergistic effects between hydrogenation catalysts and reducible metal oxide supports and provide insight into the reaction pathways responsible for their enhanced deoxygenation performance.

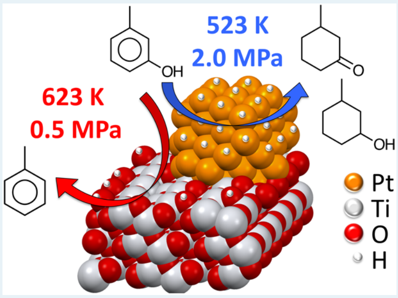

KEYWORDS: *hydrodeoxygenation, catalytic fast pyrolysis, TiO_2, m-cresol, bio-oil, DFT, hydrogen coverage, platinum*

1. INTRODUCTION

Biomass deconstruction using fast pyrolysis offers a promising route for the production of renewable bio-oil.[1−4] However, the high oxygen content of bio-oil contributes to a number of undesirable characteristics, and bio-oil must be upgraded before it is suitable for use as a drop-in transportation fuel or blendstock.[5,6] Ex situ catalytic fast pyrolysis (CFP), outlined in Figure 1, has been identified as an economically favorable approach for the production and upgrading of bio-oil.[6−9] In this process biomass undergoes fast pyrolysis, and the resulting vapors are sent to a secondary downstream reactor, where they are catalytically deoxygenated in the presence of hydrogen. Supported noble metals are attractive catalysts for ex situ CFP, since they can activate molecular hydrogen and are stable in high-steam environments. Many studies have demonstrated the utility of supported noble-metal catalysts for deoxygenation of aromatic oxygenates (e.g., phenol, cresol, guaiacol), which are representative of the lignin-derived components contained within bio-oil.[10−21] Although much has been learned from these studies, a clear understanding of the mechanistic details, role of the support, and influence of the reaction conditions has yet to be achieved.

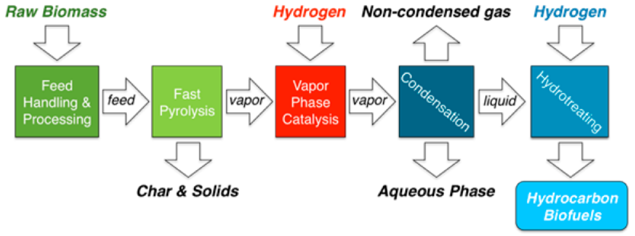

Figure 1. Process flow diagram for ex situ CFP and subsequent upgrading steps. Adapted from Ruddy et al.[6]

Molecules such as *m*-cresol are ideal model compounds to gain insight into the deoxygenation of substituted phenols, which is particularly difficult due to the high dissociation energy of the aryl−oxygen bond.[22] From a number of mechanistic investigations over a variety of catalysts, three primary reaction pathways have been proposed for this process, including ring hydrogenation followed by dehydration (HDO),[22,23] direct deoxygenation (DDO),[24,25] and tautomerization (TAU),[10,11,26,27] as shown in Figure 2.[3,6,8,10,14,15,19,22,25,28−31]

Received: December 15, 2015
Revised: March 2, 2016

DOI: 10.1021/acscatal.5b02868
ACS Catal. 2016, 6, 2715−2727

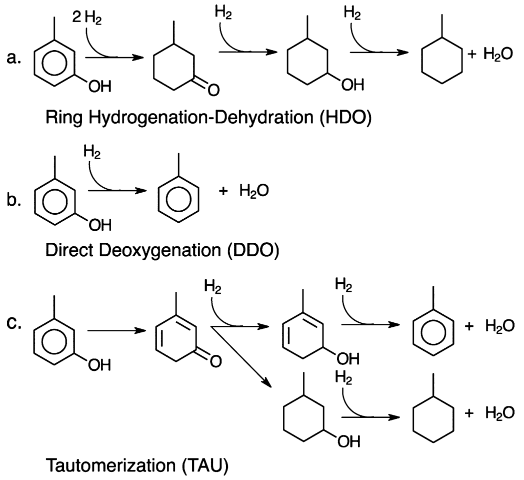

Figure 2. Proposed pathways for deoxygenation of aromatic compounds over noble-metal catalysts.

The HDO pathway, shown in Figure 2a, has been proposed as the major pathway for deoxygenation of aromatic compounds (including for *m*-cresol) over silica- and alumina-supported platinum catalysts.[23] The HDO pathway requires a bifunctional catalyst that can hydrogenate the ring and dehydrate the resulting alcohol. While this pathway is widely proposed,[6,14,19,22,25,27,28,32] computational studies using density functional theory (DFT) suggest that significant barriers exist for the initial ring hydrogenation of guaiacol and catechol over Pt(111),[10,12,23] leading to a disparity between experimental results and model predictions.

The DDO pathway, shown in Figure 2b, has been proposed for guaiacol deoxygenation over Pt/γ-Al_2O_3[14,33,34] and Pt/C.[24] Computational results from Chiu et al.[35,36] indicate that DDO is most likely to occur at step sites for a Ru catalyst. This result is consistent with findings of Lu et al., who used microkinetic modeling to show that the barrier for DDO over the Pt(111) surface was kinetically unfavorable.[12] The authors proposed that either corner and edge sites or the support contribute to deoxygenation of phenol and catechol. Other reports have also suggested that the support has the potential to influence the activity and selectivity observed during the deoxygenation of bio-oil model compounds over noble-metal catalysts.[11,14,15,23,27,31,32,37−43] Particularly interesting results have been observed over reducible metal oxides such as TiO_2, CeO_2, and ZrO_2,[10,17] where deoxygenation is hypothesized to involve oxygen vacancies.[44] These studies suggest that reducible metal oxide supports may contribute to the deoxygenation of model bio-oil compounds via a DDO mechanism at an oxygen defect site.

The TAU pathway was recently proposed by Nie and Resasco[10,11,20,26,45] and is shown in Figure 2c. This pathway involves a keto−enol tautomerization, which occurs between the hydroxyl group and the adjacent carbon−carbon double bond on the aromatic ring. The first step is the hydrogen shift from the hydroxyl group, resulting in the keto intermediate. This intermediate can then undergo hydrogenation to form either the saturated ketone or a reactive alcohol. The ketone can undergo hydrogenation−deoxygenation, while the reactive alcohol can be deoxygenated to form toluene. Experimental support for this mechanism includes the development of a kinetic model based on the TAU pathway that accurately predicts the product distribution observed during *m*-cresol deoxygenation over Pt/SiO_2.[11] Additionally, intermediates in the TAU pathway such as 2-cyclohexen-1-one have been identified using in situ diffuse reflectance infrared Fourier transform spectroscopy (DRIFTS) during deoxygenation studies of phenol over noble-metal catalysts.[10,11] For *m*-cresol deoxygenation over a Pt/SiO_2 catalyst, DFT calculations demonstrated that the TAU pathway was more energetically favorable than DDO on Pt(111), in agreement with the experimental observation that selectivity to 3-methylcyclohexanone was greater than that to toluene.[20] However, over a more oxophilic metal such as Ru(0001), DFT calculations indicated that DDO was favored, and toluene was the dominant reaction product observed experimentally.[20] The importance of oxophilicity on the TAU pathway is consistent with a study by Hensley et al.,[46,47] which reported that the keto−enol isomerization of phenol over the oxophillic base metal Fe(110) surface proceeds with a high barrier of 1.83 eV.[46]

Development of an overarching mechanism is also complicated by varying reaction conditions employed during the deoxygenation of pyrolysis vapors. For example, ex situ CFP requires higher temperatures (573−723 K) and lower pressures (0.1−1 MPa) than typical deoxygenation via hydrotreating (HT; 473−573 K, 1−20 MPa).[6] The resulting differences in surface coverage of hydrogen and substrate as well as thermodynamic and kinetic limitations will likely influence the dominant reaction pathways. Indeed, recent reports demonstrate that the reaction temperature plays an important role in determining the product distribution from deoxygenation of bio-oil model compounds over noble-metal catalysts. At temperatures ≤523 K, ring hydrogenation is favorable and saturated products are produced with high selectivity; however, at temperatures above 523 K, hydrogenation activity decreases and the production of aromatic products increases.[13−15,18,23,48−50] Shifts in the thermodynamic equilibrium at higher temperature may contribute to these differences.[6] However, the limited amount of directly comparable data makes definitive conclusions difficult, and a better understanding of catalyst behavior under these two conditions is critical to understand the product distribution obtained during the deoxygenation of pyrolysis vapors.

Previous experimental and computational studies have not yet arrived at a clear mechanism for aromatic deoxygenation, and it is likely that multiple routes contribute to the observed catalyst reactivity. Further investigation is necessary to gain a better understanding of the influence of reaction conditions, mechanistic details, and role of the support. To that end, here we present a combined experimental−computational investigation into the deoxygenation of the model compound *m*-cresol over Pt/C and Pt/TiO_2 catalysts. Each catalyst was evaluated in a gas-phase flow reactor under temperatures and pressures relevant to ex situ CFP (623 K, 0.5 MPa) and HT (523 K, 2.0 MPa). Computational modeling was conducted over a hydrogen-covered Pt(111) surface to better understand the transformations that occur over the metallic phase and over an oxygen vacancy on the TiO_2(101) surface to gain insight into energetically accessible pathways over reducible metal oxide supports. A combination of the experimental and computational results was used to develop a reaction network that incorporates the influence of reaction conditions and the role of the support during *m*-cresol deoxygenation. The computational results indicate that the most energetically favorable pathway is ring hydrogenation to 3-methylcyclohexanone and 3-methylcyclohexanol over Pt(111), while deoxyge-

DOI: 10.1021/acscatal.5b02868
ACS Catal. 2016, 6, 2715−2727

nation via tautomerization and direct deoxygenation may proceed over $TiO_2(101)$ with slightly higher barriers. These findings, which are consistent with the experimentally observed product selectivities, suggest that the reactivity of Pt/TiO_2 and Pt/C is driven by the metallic phase at 523 K while contributions from the TiO_2 support enhance deoxygenation at 623 K.

2. RESULTS

2.1. Catalyst Synthesis and Characterization. The Pt catalysts were prepared by typical incipient wetness methods and reduced at 723 K prior to catalytic characterization. The X-ray diffraction (XRD) patterns of the reduced Pt/C and Pt/TiO_2 are given in Figure 3. In both cases, the characteristic diffraction pattern of crystalline Pt is evident. The titania used in this report is a mixed-phase material consisting of primarily the anatase phase, with a lesser portion of rutile (small peaks at 27 and 36°, Figure 3a). In addition to Pt diffractions, the Pt/C material consists of graphitic carbon and minor contributions from other crystalline phases associated with the carbon support (Figure 3b). A diffractogram of the carbon support in the absence of Pt is presented in Figure S1 in the Supporting Information.

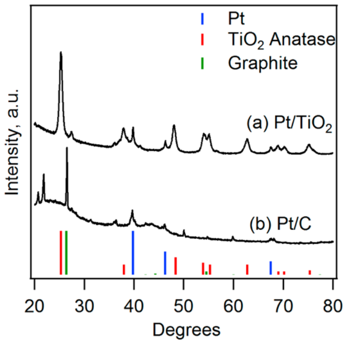

Figure 3. XRD patterns of (a) Pt/TiO_2 and (b) Pt/C with reference peaks for Pt, anatase TiO_2, and graphite. The small peaks at 27 and 36° in (a) are attributed to diffractions from rutile TiO_2.

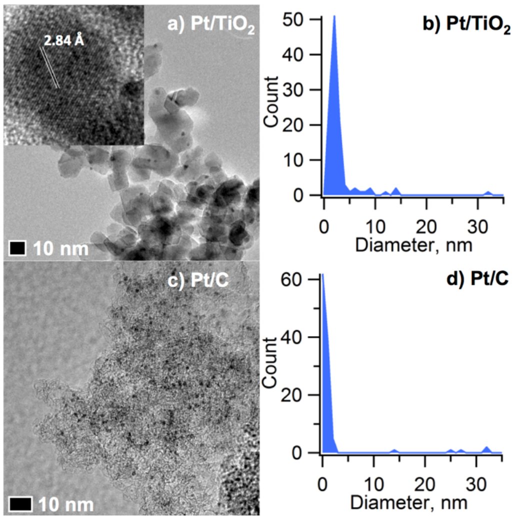

Figure 4. TEM images and particle size distributions for Pt/TiO_2 (a, b) and Pt/C (c, d). A high-magnification inset in (a) shows the measured lateral spacing between Pt atoms.

Table 1. Pt/TiO_2 and Pt/C Metal Loading, CO Uptake, Dispersion, Average Crystallite Size, and Average Particle Diameter Determined by CO Chemisorption, XRD, and TEM

catalyst	metal loading, wt %	CO uptake, μmol g_{cat}^{-1}	dispersion, %
Pt/C	4.32	87.9	39.4
Pt/TiO_2	4.8	26.7	10.9

particle size, nm			
chemisorption	XRD, crystallite size	TEM, surface area weighted	TEM, volume weighted
4.1	26.4	28.2	29.9
15.2	24.4	17.5	26.7

Transmission electron microscopy (TEM) images and the corresponding particle size distribution for Pt/TiO_2 and Pt/C are shown in Figure 4. The majority of the particles observed were spherical, although a small number of elongated particles were present on both catalysts. A micrograph showing the spherical shape of a platinum particle on titania is provided in Figure S2 in the Supporting Information. In comparison to the Pt/TiO_2 catalyst, Pt/C exhibited lower polydispersity in size in the vicinity of the average (0−5 nm) but contained a greater number of large particles (>20 nm). An inset provided in Figure 4a shows a high-magnification micrograph of Pt/TiO_2. The lateral spacing of Pt atoms in this image was 2.84 Å, which is in agreement with the surface lattice constant of Pt(111) determined via scanning tunneling microscopy (2.80 Å) and density functional theory calculations (2.83 Å).[51] Carbon-supported Pt particles are also known to adopt a truncated-octahedral geometry with predominately (111) sites exposed at diameters >2 nm.[52,53] The BET surface areas of the carbon and TiO_2 supports were determined to be 960 and 95 $m^2\ g^{-1}$, respectively. The NH_3-TPD profile from each support is provided in Figure S3 in the Supporting Information and indicates an acid site density of 53 μmol g^{-1} for carbon and 490 μmol g^{-1} for TiO_2. The metal loading, carbon monoxide uptake, dispersion, average crystallite size, and average particle diameter according to chemisorption, XRD, and TEM are shown in Table 1. CO chemisorption carried out over TiO_2 and carbon in the absence of Pt exhibited no detectable CO uptake. The average crystallite sizes determined by XRD line broadening agree reasonably well with the volume-weighted TEM measurements and are primarily influenced by contributions from the largest particles. The average particle sizes determined by CO chemisorption are lower than the surface-weighted TEM measurements, particularly for the Pt/C catalyst. This apparent discrepancy may be due to the presence of small particles (<2 nm) that contribute to CO uptake but are unable to be observed by TEM and are expected to minimally influence the crystallite size determined by XRD, which is volume-weighted. The increased dispersion of Pt/C relative to Pt/TiO_2 according to CO chemisorption is consistent with a previous study and is likely a result of the high surface area of the carbon support.[17] Although the Pt particle sizes are different on the carbon- and TiO_2-supported catalysts, previous reports demonstrated that metal dispersion does not significantly affect the product distribution observed during the deoxygenation of phenol and *m*-cresol over Pd/ZrO_2.[10,45] It has also been demonstrated that the presence of reducible metal oxide supports increases the intrinsic deoxygenation activity of noble metals regardless of their dispersion.[45] While it remains possible that particle size effects influence the reactions in this report, their contributions are expected to be minimal.

2.2. Catalyst Testing. The carbon selectivity and turnover frequency (TOF) for each catalyst is compared at 35% (±3%) conversion in Figure 5. It is possible that the selectivity and activity may be affected by product inhibition at 35% conversion, and the data in Figure 5 are not intended to directly reflect intrinsic catalytic properties. Instead, they provide a comparative assessment of the activity and selectivity observed over each catalyst at a similar level of conversion. Toluene was the dominant product for both catalysts under ex situ CFP conditions, accounting for 78% and 46% of the carbon selectivity over Pt/TiO_2 and Pt/C, respectively. Under HT conditions, 3-methylcyclohexanone and 3-methylcyclohexanol were highly favored and accounted for >95% of the carbon selectivity. Methylcyclohexane was detected under both conditions but was a minor product formed with <11% of the carbon selectivity in all cases. These data are in agreement with the thermodynamic concepts summarized by Ruddy et al.,[6] which suggests that ring hydrogenation reactions are favorable at low temperature (473−523 K) while other reactions such as DDO and acid-catalyzed transformations are activated above 523 K.[6] In terms of TOF, both catalysts were more active under HT conditions, and Pt/TiO_2 exhibited more than double the activity of Pt/C under comparable conditions.

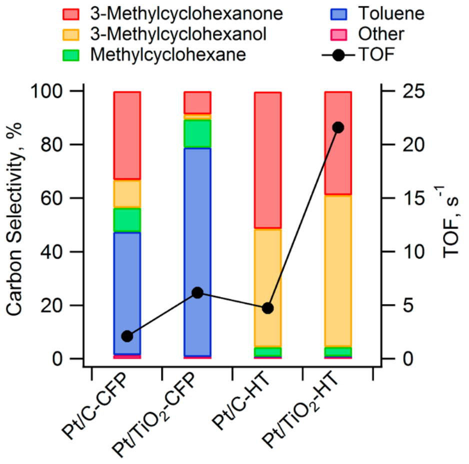

Figure 5. Carbon selectivity and TOF for each catalyst compared at 35% conversion (±3%) under ex situ CFP (623 K, 0.5 MPa) and HT (523 K, 2.0 MPa) conditions.

The carbon selectivities and conversions at weight hourly space velocities (WHSV) from 200 to 700 h^{-1} are presented in Figure 6. The data shown for each catalyst and set of conditions were collected during a single experiment and are based on an average of two samples taken at 50 min increments. The variance between the duplicate samples is not expected to be a function of WHSV, and the error associated with these

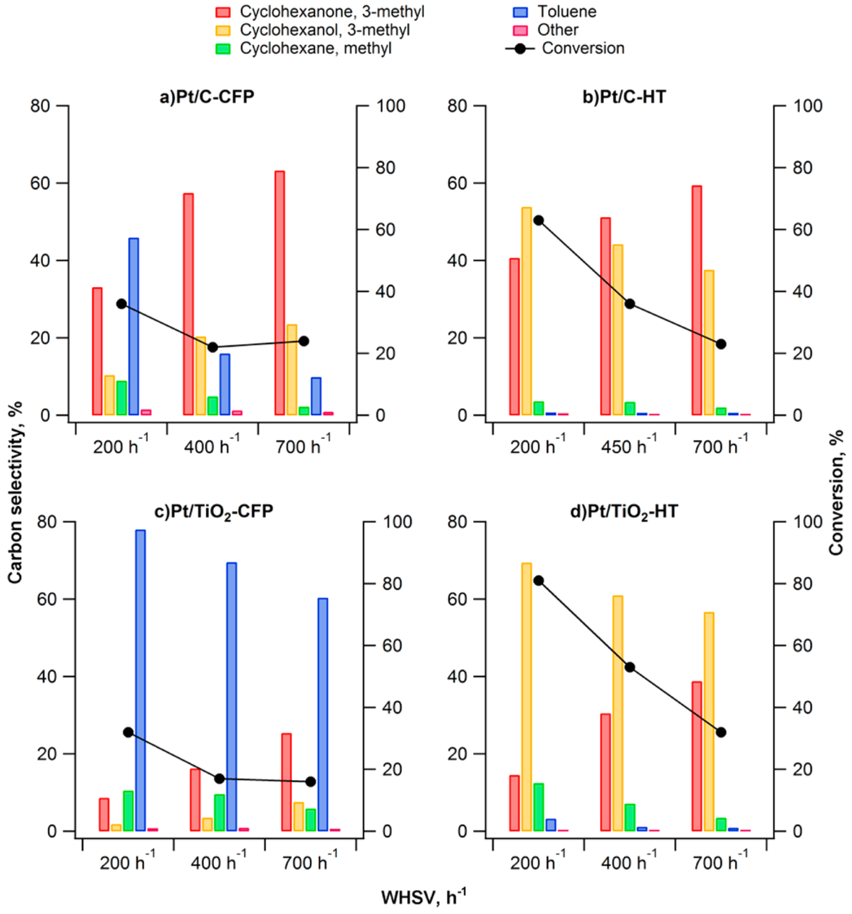

Figure 6. Carbon selectivities (colored bars) and conversions (black circles) as a function of WHSV for (a) Pt/C−CFP, (b) Pt/C-HT, (c) Pt/TiO_2-CFP, and (d) Pt/TiO_2-HT. Ex situ CFP conditions correspond to 623 K and 0.5 MPa, while HT conditions correspond to 523 K and 2.0 MPa.

measurements was estimated by calculating the pooled standard deviation of the six samples collected within a single experiment. In all cases, the pooled standard deviation was <6%. The results of separate experiments shown in Figure S4 in the Supporting Information suggest that both catalysts are highly stable, and any effect of catalyst deactivation on the data presented in Figure 6 is expected to be minimal. The selectivity to 3-methylcyclohexanone increased as conversion decreased for both catalysts and conditions. This result suggests that 3-methylcyclohexanone is a primary product. This assignment is consistent with a previous report in which 3-methylcyclohexanone was identified as a primary product during the deoxygenation of *m*-cresol over Pt/SiO_2 at 573 K and atmospheric pressure.[20] Unlike the case for 3-methylcyclohexanone, the selectivity to 3-methylcyclohexanol increased with increasing conversion under HT conditions. This result is consistent with the sequential HDO reaction pathway shown in Figure 2a, in which the aromatic ring is hydrogenated to form a ketone, followed by hydrogenation to a saturated alcohol.[6,48] The selectivity toward the deoxygenated products methylcyclohexane and toluene was greater over Pt/TiO_2 in comparison to Pt/C under both conditions, particularly at the highest conversion. For example, under HT conditions the combined selectivity to methylcyclohexane and toluene at a WHSV of 200 h^{-1} was 16 and 4.4 for Pt/TiO_2 and Pt/C, respectively.

2.3. Calculated Mechanisms. To examine the aromatic deoxygenation reaction mechanisms, calculations were performed to identify energetically favorable pathways over the Pt(111) and anatase $TiO_2(101)$ surfaces (Scheme 1). The contributions from carbon are expected to be minimal, as it is considered to be an inert support for deoxygenation reactions under the conditions explored here.[54] Pathways over the Pt(111) surface include coadsorbed hydrogen for the ring hydrogenation steps of the HDO and TAU mechanisms to account for surface crowding. To explore the effect of the reducible metal oxide support, the DDO and TAU mechanisms were calculated over an oxygen vacancy on the $TiO_2(101)$ surface.

Scheme 1. Reaction Pathways for *m*-Cresol Hydrogenation and Deoxygenation That Were Computationally Investigated over Pt and TiO_2 Surfaces

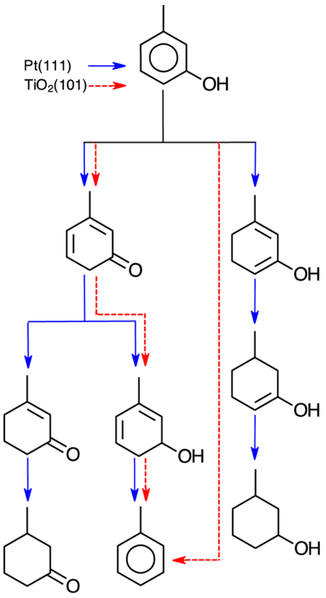

2.3.1. Pt(111) Surface. The HDO mechanism over the Pt(111) surface (Pt-HDO) is shown in Scheme 2a and results in the formation of 3-methylcyclohexanol (structure TH_4), which has a significantly weakened C−O bond energy relative to *m*-cresol. The potential energy surface (PES) for the Pt(111) reaction steps is shown in Figure S5 in the Supporting Information. The barrier relative to the starting structure R_1 over the hydrogen-covered Pt(111) surface is 0.69 eV for the formation of 3-methylcyclohexenol, denoted RH_1-RH_2. The RH_2 structure can undergo tautomerization to the TH_3 structure. A similar tautomerization reaction, forming a slightly different intermediate, would also be possible starting at RH_1. However, the difference in the barriers between RH_1-RH_2 and RH_2 to TH_3 is only 0.06 eV. Therefore, this change is unlikely to affect the overall reaction. While a third hydrogenation step is possible from RH_2, this reaction results in an endothermic structure and would require rearrangement of the hydroxyl group from the axial to the lower energy equatorial position. The TH_3 and TH_4 structures are nearly degenerate, with a negligible interconversion barrier. Therefore, the TH_3 structure can convert to the TH_4 alcohol on the basis of hydrogen availability and thermodynamic equilibrium. The final TH_4 to P_2 barrier is the highest in this pathway (and all pathways in this report) at 1.23 eV and is endothermic by 1.14 eV. An alternative route for this C−O bond breaking is a reaction at a defect, corner, edge, or step site on the Pt surface, which has been demonstrated for Ru surfaces.[35,36] In addition, reactions that involve the support may also be possible (vide infra). The structures and reaction profiles for Pt-HDO are shown in Figures S6−S10 in the Supporting Information.

Scheme 2. (a) Pt-HDO, (b) Pt-TAU, and (c) Pt-TAU-HDO Mechanisms over the Hydrogen-Covered Pt(111) Surface[a]

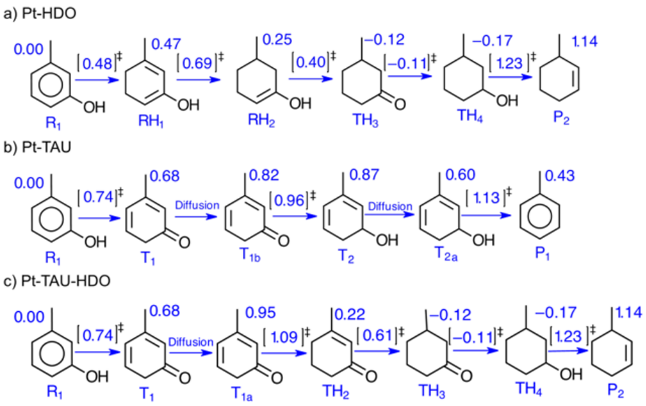

[a] All energies are in eV and are referenced to R_1.

The Pt-TAU pathway is presented in Scheme 2b. The first step in this reaction is simultaneous hydrogen transfers from the surface to the *β*-carbon (relative to the hydroxyl group) and from the hydroxyl group to the Pt(111) surface. A schematic for the enol to keto intermediate is shown in Figure 7. Stepwise transfer of hydrogen between the *β*-carbon and the surface was not found to be stable during optimization with the hydrogen-covered surface. The highest barrier in this pathway is the removal of the hydroxyl group by the Pt(111) surface, step T_2-P_1, with a barrier of 1.13 eV. The first diffusion for this pathway corresponds to a correction to account for differences in the

DOI: 10.1021/acscatal.5b02868
ACS Catal. 2016, 6, 2715−2727

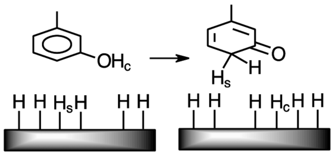

Figure 7. Hydrogen shift for the tautomerization of *m*-cresol over a hydrogen-covered Pt(111) surface.

hydrogen number between this state and the reference. This correction corresponds to the addition of 1/2 H_2 and the H-defect formation energy, while the second corrects only for H-defect formation present in the reactant. The relatively high C−O bond dissociation barrier and endothermic reaction energy are consistent with the low percentage of deoxygenation seen in Figures 5 and 6 for the Pt/C catalyst. The structures and reaction profiles for these steps are shown in Figures S11−S13 in the Supporting Information.

The HDO mechanism is also possible starting from intermediates in the tautomerization pathway denoted Pt-TAU-HDO.[11] In this pathway, after the initial tautomerization step, the ring is hydrogenated, resulting in TH_2. As can be seen in Scheme 2c, the highest barrier for the first ring hydrogenation, step T_1-TH_2, is 1.09 eV. The second hydrogenation, TH_2-TH_3, is endothermic by 0.22 eV relative to the reactants. The deoxygenation barrier is high and exothermic as mentioned above. The structures and reaction profiles for these steps are shown in Figures S14 and S15 in the Supporting Information.

2.3.2. TiO_2(101) Surface.

Deoxygenation of *m*-cresol over TiO_2(101) is hypothesized to be an inverse Mars−van Krevelen (MvK) process at oxygen-vacancy defects.[44] The experimental results reported here indicate that no activity is observed over anatase TiO_2 in the absence of Pt. This is likely due to passivation of the oxygen vacancies during the initial phase of the reaction. As such, a mechanism for regenerating the vacancies must be present.[44,55] Spillover of hydrogen from the metallic phase is the most likely source of hydrogen.[55,56] While the barrier for spillover was not calculated due to uncertainty associated with the morphology of the interface, the barriers for hydrogen activation at high coverage over Pt(111) and hydrogen diffusion over the TiO_2(101) surfaces were explored. The barrier for hydrogen dissociation is less than the physisorption of molecular hydrogen on the Pt(111) surface even at high coverage (7:8 ratio of hydrogen to surface sites). Diffusion of atomic hydrogen over the anatase TiO_2(101) surface was calculated to be 0.6 eV. This value is in agreement with previous studies on the diffusion of hydrogen on rutile TiO_2 that reported a similar barrier of 0.56 eV.[55] The PES for the reactions of *m*-cresol over the TiO_2(101) surface is shown in Figure S16 in the Supporting Information.

The inverse MvK mechanism for the DDO of *m*-cresol at the oxygen vacancy sites (Ti-DDO) occurs by directly breaking the aryl−oxygen bond as shown in Scheme 3a.[38,44,57,58] This mechanism was investigated over the TiO_2(101) surface with a single oxygen vacancy by directly breaking the aryl−oxygen bond while eliminating the oxygen defect. The hydrogen addition to the aryl carbon comes from either a surface hydroxyl group or from intramolecular transfer from the hydroxyl group. The reference state for this reaction contains an oxygen defect. The structures and reaction profiles for these steps are shown in Figure S17 in the Supporting Information.

Scheme 3. (a) TiO_2-DDO (b) and TiO_2-TAU Mechanisms over the TiO_2(101) Surface[a]

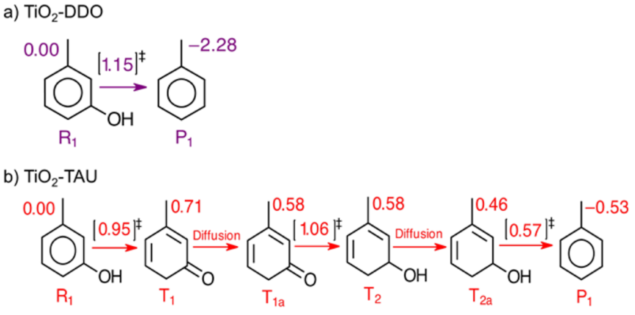

[a] All energies are in eV and are referenced to R_1.

The Ti-TAU mechanism can occur in the same manner as the Pt-TAU mechanism. In the Ti-TAU mechanism, shown in Scheme 3b, tautomerization occurs entirely over the TiO_2(101) surface with the same three steps of the Pt-TAU mechanism: namely, tautomerization, alcohol formation, and deoxygenation. The first diffusion step, shown in Scheme 3b, T_1 to T_{1a}, is the addition of a hydrogen atom to the surface with the energy of the hydroxyl group removed. The highest barrier to tautomerization over the TiO_2(101) surface is shown in Scheme 3b, step T_{1a} to T_2, with an energy of 0.95 eV and is higher than the Pt(111) surface by 0.21 eV. The energy barrier is essentially degenerate with the Pt-TAU-HDO mechanism. The final step in Scheme 3b, T_{2a} to P_1, is shown as a single step but occurs in two steps. Since the barrier of the second step is below the reaction energy of the first step, only the barrier for the first step is shown. The final step is the C−O bond breaking. Since this step starts from the reactive alcohol T_2, the barrier is 0.58 eV lower than for the aryl−oxygen bond of *m*-cresol and 0.66 eV lower than the C−O bond breaking of 3-methylcyclohexanol. The structures and reaction profiles for these steps are shown in Figures S18−S21 in the Supporting Information.

The reaction network and PES for the overall reaction is shown in Figure 8. The reaction network indicates all structures and barriers relative to the reactant R_1, and the surface state for each set of reactions is indicated by color. The PES for the entire reaction set indicates the most likely observed products under HT conditions and the routes for deoxygenation under CFP conditions.

3. DISCUSSION

3.1. Reactions over Pt. The reaction network in Figure 8 suggests that the minimum energy pathway over Pt(111) leads to formation of 3-methylcyclohexanone and 3-methylcyclohexanol via the Pt-HDO mechanism. This result is consistent with the experimental results shown in Figures 5 and 6 collected under HT conditions. Deoxygenation of 3-methylcyclohexanol would not be expected over the Pt(111) surface, as it has a high overall barrier of 1.23 eV. However, it is possible that deoxygenation of the saturated alcohol to form methylcyclohexane could occur at undercoordinated sites, as has been previously demonstrated over Ru catalysts.[35,36]

In addition to the reaction barriers, hydrogen availability and surface crowding are important variables that may affect the accessible reaction pathways. Previous studies predict that the Pt(111) surface would be covered with a full monolayer (ML) of hydrogen under HT conditions, while under ex situ CFP

DOI: 10.1021/acscatal.5b02868
ACS Catal. 2016, 6, 2715−2727

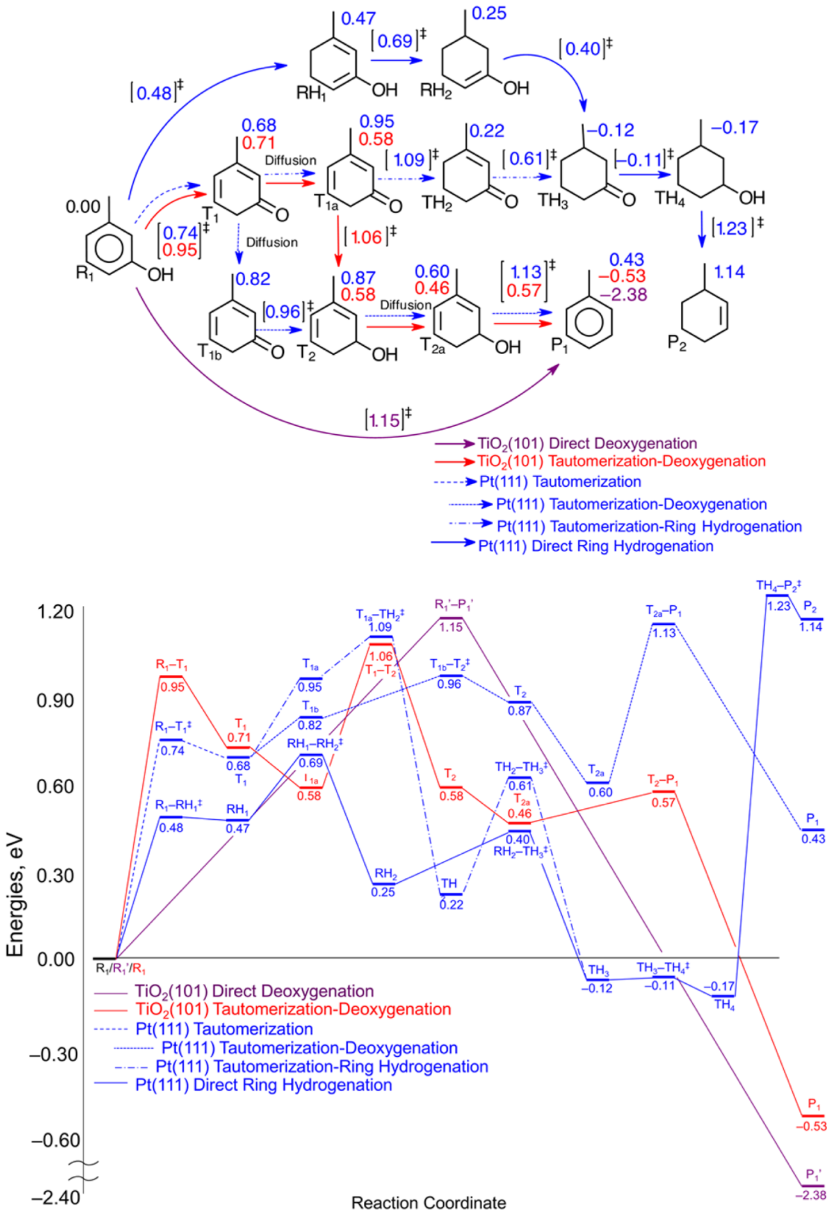

Figure 8. Reaction network (top) and PES (bottom) for reaction steps occurring over the Pt(111) metallic phase and the $TiO_2(101)$ support. The barrier heights are labeled with ‡, and energies without labels are reaction energies. All energies are in eV and are referenced to R_1.

conditions the hydrogen coverage could vary from 1 to 0.5 ML on the basis of the error in the calculated energies and uncertainty of entropic contributions.[59,60] The reduction in hydrogen coverage under ex situ CFP conditions may reduce the favorability of the Pt-HDO pathway due to its high hydrogen requirement. This is supported by previous computational work in which the hydrogenation barriers of catechol (1.23 eV)[10] and phenol (0.94 eV)[61] over a Pt(111) surface with a single hydrogen adsorbate were shown to be high and endothermic. In this case, other reaction pathways over Pt(111) may become significant. Included in these pathways is Pt-TAU, shown in Scheme 2b and Figure 8. This mechanism is similar to that proposed by Tan et al.[20] in which *m*-cresol deoxygenation proceeds through a tautomerization step over bare Pt and Ru catalysts, resulting in the formation of 3-methylcyclohexanone. In the current work, deoxygenation via the Pt-TAU mechanism is higher in energy than ring hydrogenation through the Pt-HDO mechanism by 0.43 eV. However, if hydrogen availability is low and the barriers are accessible at higher temperatures, then the Pt-TAU mechanism may occur, resulting in deoxygenation to form toluene. These findings are consistent with the experimental results in Figures 5 and 6, which show high selectivity to toluene under ex situ CFP conditions.

The interconversion between cycloalkanes and aromatics over Pt catalysts is well documented, and it is possible that some toluene is produced from the dehydrogenation of methylcyclohexane.[28,79−81] In order to understand how thermodynamic limitations affect this process, the equilibrium constant for the reaction of methylcyclohexane to toluene and hydrogen was determined as a function of temperature, as shown in Figure 9. At 523 K, methylcyclohexane is thermodynamically favored, while at 623 K toluene becomes thermodynamically favorable. The approach to equilibrium based on the molar ratios of toluene to methylcyclohexane observed during each experiment is presented in Table 2. Values in excess of 1 are likely due to error associated with the

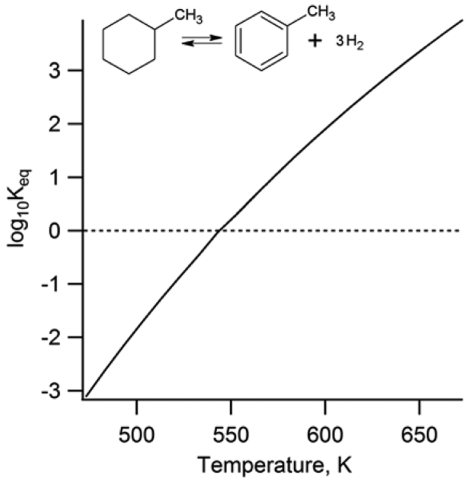

Figure 9. Equilibrium constant for the reaction of methylcyclohexane to give toluene and hydrogen plotted as a function of temperature. The K_{eq} values were determined by integrating the van't Hoff equation from the standard state to each temperature. Standard state enthalpies, standard molar entropies, and heat capacity data as a function of temperature fit to third-order polynomials were obtained from the NIST. A $\log_{10} K_{eq}$ value equal to 0 corresponds to a K_{eq} value of 1.

Table 2. Approach to Equilibrium Based on the Ratio of Toluene to Methylcyclohexane Observed during Each Experiment

	approach to equilibrium		
catalyst/support, conditions	200 h^{-1}	400/450 h^{-1}	700 h^{-1}
Pt/C, HT	0.89	0.81	1.4
Pt/TiO_2, HT	1.1	0.67	1.1
Pt/C, CFP	0.034	0.022	0.029
Pt/TiO_2, CFP	0.049	0.047	0.067

quantification of small amounts of toluene, which accounted for <1.0% of the carbon selectivity under HT conditions. At these concentrations, small discrepancies in the analytical methods can have a large effect on the resulting ratios. Despite the uncertainties in this measurement, it is clear that the conversion of methylcyclohexane to toluene may be thermodynamically limited under HT conditions. However, under ex situ CFP conditions, no thermodynamic constraint is imposed. The formation of toluene via the Pt-HDO pathway under ex situ CFP conditions is consistent with the results presented in Figure 6, which show high selectivity to toluene coupled with increasing selectivity to 3-methylcyclohexanone at lower conversion, suggesting that it is a primary product. Consequently, it is possible that both the Pt-HDO and Pt-TAU pathways contribute to the production of toluene under ex situ CFP conditions.

The tautomerization of *m*-cresol is a step in both the Pt-TAU and Pt-TAU-HDO mechanisms, but the reaction mechanism presented here differs significantly from previous computational reports on Pt(111) and Fe(110) surfaces. The barrier resulting from gas-phase intramolecular hydrogen transfer (no surface) has been reported to be 2.29 eV. In a separate study on Pt(111),[61] in which the surface was included in the hydrogen transfer step, the barrier was significantly reduced to 1.17 eV. A reduction in the tautomerization barrier with surface participation was also observed in the work by Tan et al.[20] Thus, surface participation in the hydrogen transfer reaction significantly lowers the barrier. In the Pt-TAU mechanism presented in this study, which includes both surface participation and surface hydrogen, the tautomerization barrier was found to be 0.74 eV. This low barrier indicates that the presence of coadsorbed hydrogen would significantly enhance the favorability of *m*-cresol tautomerization over Pt(111).

3.2. Reactions over TiO_2. The experimental results presented in Figure 5 show that Pt/TiO_2 exhibits greater activity and higher selectivity to toluene than does Pt/C. The increased TOF and enhanced selectivity toward deoxygenated products observed over Pt/TiO_2 relative to Pt/C are consistent with a previous report in which Ru/TiO_2 exhibited activity and selectivity to aromatic products greater than that of Ru/SiO_2, Ru/Al_2O_3, and Ru/C for guaiacol deoxygenation at atmospheric pressure and 673 K.[17] The Ru-based results were attributed to synergistic metallic phase−support interactions in which Ru facilitated the reduction of TiO_2, creating oxygen vacancies that were highly active for deoxygenation. Similar results have been reported for other metal/reducible oxide catalysts and metal-free reducible oxide catalysts.[44,45] For

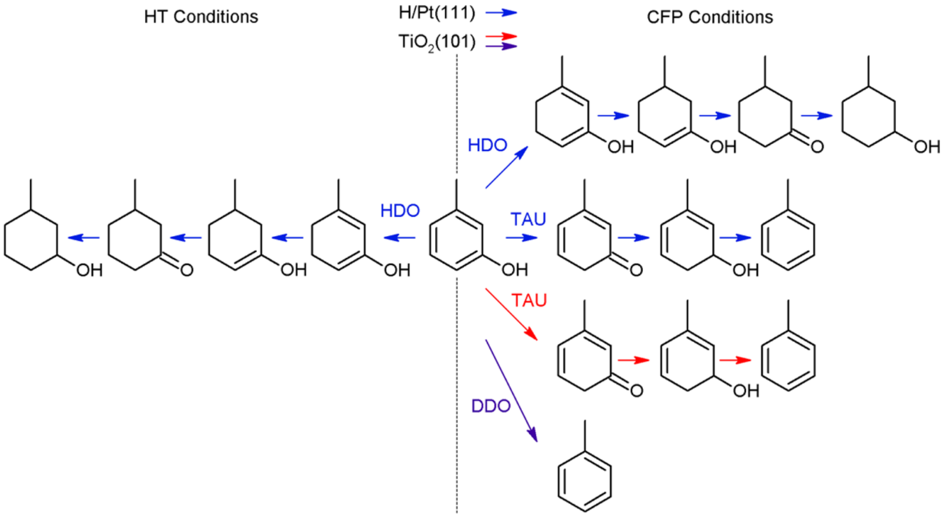

Figure 10. *m*-Cresol deoxygenation pathways accessible for Pt/C and Pt/TiO_2 catalysts under HT (523 K, 2.0 MPa) and CFP conditions (623 K, 0.5 MPa) at high hydrogen coverage.

example, during the deoxygenation of phenol at 573 K and atmospheric pressure, benzene production was promoted over Pd/ZrO_2, while Pd/Al_2O_3 and Pd/SiO_2 favored the formation of cyclohexanone. The increased benzene selectivity was attributed to oxophilic Zr^{4+} sites on the surface of the support.[10] Similarly, Schimming et al. correlated the conversion of guaiacol with the concentration of oxygen vacancies over a ceria−zirconia catalyst.[44] Other calculations over 10-atom Ru clusters with no hydrogen on a rutile h-$TiO_2(110)$ indicate an interesting alternate mechanism related to the amphoteric nature of the support.[62]

These experimental data are supported by the computational results presented in this report. Reaction pathways for DDO and TAU shown in Scheme 3 over the $TiO_2(101)$ surface provide additional pathways for deoxygenation. The barriers for these reactions are 1.06 eV for Ti-TAU (step T_{1a}-T_2) and 1.15 eV for Ti-DDO (step R_1-P_1). These barriers are similar to previous calculations at sulfur-defect sites in sulfided MoS_2 and CoMoS catalysts, with reported barriers of 1.04 and 1.14 eV, respectively.[57] The Ti-DDO and Ti-TAU barriers are higher than the Pt-HDO mechanism barrier (0.69 eV, step RH_1-RH_2) proposed to occur over the metallic phase. These results suggest that the reactivity of Pt/TiO_2 and Pt/C is likely driven by the metallic phase at low temperature (HT conditions), as discussed above. At the higher temperature of ex situ CFP, these barriers become accessible, resulting in increased deoxygenation from the TiO_2 support. It is important to note that the barrier for oxygen vacancy formation via a spillover mechanism was not directly calculated, and therefore it is not possble to determine if the oxygen defect formation is the highest barrier in this pathway. Our results suggest that the Ti-DDO and Ti-TAU mechanisms occur if these defects are present.

3.3. Combined Reaction Mechanism.

A reaction mechanism is proposed in Figure 10 and suggests that the Pt-HDO pathway is accessible to Pt/TiO_2 and Pt/C under both conditions. Under ex situ CFP conditions, Pt can facilitate deoxygenation to methylcyclohexane and dehydrogenation to toluene. The Pt-TAU pathway may also be accessible under ex situ CFP conditions and results in the production of toluene. Additional pathways over the TiO_2-supported catalyst also contribute to the observed reactivity, especially under ex situ CFP conditions. These include DDO and TAU, which result in the production of toluene.

It is also possible that deoxygenation reactions can occur in two steps with one occurring over the metallic phase and the other occurring over the support, in anaology to ring hydrogenation−dehydration over hydrogen-activating metals on acidic supports: e.g., Pt/Al_2O_3.[6] In this work the barrier for DDO of 3-methylcyclohexanol at an oxygen vacancy on the $TiO_2(101)$ surface is 0.71 eV, as shown in Scheme 4. This possibility is consistent with a previous study in which the enhanced deoxygenation activity of Ru/TiO_2 was attributed to an interface effect.[17,38] Similar effects may contribute to the enhanced activity of Pt/TiO_2 under HT conditions observed in this work, as shown in Figure 5. Thus, it is possible that under conditions which favor ring hydrogenation a more reducible metal oxide could drive deoxygenation. However, a more detailed theoretical and experimental understanding of the active phase−support interface is necessary to determine if this possibility is feasible.

Scheme 4. Intrinsic Barriers of 3-Methylcyclohexanol DDO at Defect Sites in the $TiO_2(101)$ Surface

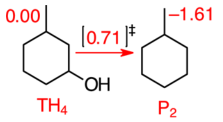

4. CONCLUSIONS

The activity and selectivity observed during the deoxygenation of m-cresol over Pt catalysts is dependent on the choice of support and reaction conditions. Computational modeling identified ring hydrogenation to 3-methylcyclohexanone and 3-methylcyclohexanol as the most energetically favorable pathway over Pt(111). Over $TiO_2(101)$, tautomerization and direct deoxygenation to toluene were identified as additional energetically favorable routes. These findings are consistent with the experimental results, in which Pt/TiO_2 was more active on a metal site basis and exhibited higher selectivity to toluene than did Pt/C. The influence of reaction conditions was demonstrated by the increased selectivity to toluene observed under ex situ CFP conditions (623 K, 0.5 MPa) relative to HT conditions (523 K, 2.0 MPa), which is thought to be associated with thermodynamic limitations imposed on the conversion of cycloalkanes to aromatics under HT conditions. The combined experimental−computational results reported here highlight the synergistic effects between hydrogenation catalysts and reducible metal oxide supports and provide insight into the reaction pathways responsible for their enhanced deoxygenation performance. Additional investigations into reactions at the metal−oxide interface, while beyond the scope of this study, could provide significant insight and further improvement in catalytic performance.

5. EXPERIMENTAL MATERIALS AND METHODS AND COMPUTATIONAL METHODS AND MODELS

5.1. Materials.

TiO_2 (Aeroxide P90) was obtained from Evonik, and carbon (DARCO activated charcoal) was obtained from Sigma-Aldrich. Both supports were used as received. $Pt(NH_3)_4(NO_3)_2$ was obtained from Strem Chemicals and used as received. Crushed quartz (150−250 and 300−425 μm, Powder Technologies Inc.) and silicon carbide (177−250 μm, McMaster Carr) were used as diluent materials for reactor testing. m-Cresol (99%) was obtained from Sigma-Aldrich and used as received. Certified gas blends (5% argon/95% hydrogen and 1% oxygen/99% helium) were obtained from Air Liquide. Hydrogen (UHP, General Air), and nitrogen (house supply) were also utilized.

5.2. Catalyst Synthesis.

Carbon- and TiO_2-supported Pt were prepared from $Pt(NH_3)_4(NO_3)_2$ via standard incipient-wetness impregnation methods. For Pt/TiO_2, 14.25 mL of an aqueous solution of $Pt(NH_3)_4(NO_3)_2$ corresponding to a 5.0 wt % metal loading was added dropwise to 9.5 g of TiO_2. For Pt/C, 23.75 mL of an aqueous solution of $Pt(NH_3)_4(NO_3)_2$ corresponding to a 5.0 wt % metal loading was added dropwise to 9.5 g of carbon. The impregnated materials were dried at 323 K overnight in an oven and reduced in the reactor at 723 K under flowing molecular hydrogen. Catalyst samples used for characterization were also reduced at 723 K prior to analysis. These conditions were selected on the basis of literature values and have been shown to achieve complete reduction of supported Pt.[63,64]

DOI: 10.1021/acscatal.5b02868
ACS Catal. 2016, 6, 2715−2727

5.3. Catalyst Characterization. Powder XRD data were collected using a Rigaku Ultima IV diffractometer with a Cu Kα source (40 kV, 44 mA). Diffraction patterns were collected in the 2θ range of 20−80° at a scan rate of 4° min^{-1}. Samples (10−20 mg) were supported on a glass sample holder with a 0.2 mm recessed sample area and were pressed into the recession with a glass slide to obtain a uniform z axis height. Data were compared to reference card files from the International Center for Diffraction Data (Pt, 00-004-0802; graphite, 00-008-0415; TiO$_2$-anatase, 00-001-0562, TiO$_2$-rutile, 00-001-1292) to confirm the identity and phase of the sample. The average crystallite size, which is analogous to the volume-weighted apparent particle size, was calculated from XRD peak broadening of the supported catalysts using the Scherrer equation on the basis of the Pt(111) diffraction.

Active site density and metal dispersion for Pt/C and Pt/TiO$_2$ were measured from CO pulse chemisorption performed using an Altamira AMI-390 microflow reactor system equipped with a thermal conductivity detector (TCD). Samples (ca. 180 mg) were loaded in a quartz U-tube reactor and heated under 10% H$_2$/Ar to 723 K at 5 K min^{-1} with a hold time of 2 h. After the reduction step, catalyst samples were flushed with He (50 mL min^{-1}) for 30 min to remove adsorbed hydrogen. The samples were then cooled to 303 K and dosed with 500 μL pulses of a 10% CO/He mixture. Saturation of the sample was achieved when the peak areas of two consecutive pulses were within ±4% and was generally within three to eight pulses. A sample loop of known volume (500 μL corresponding to 1.65 μmol of CO under the operating conditions) was used to calibrate the TCD response for CO. The site density was determined by assuming a stoichiometry of one CO molecule adsorbed per active site and used to calculate the average particle size, which is analogous to the surface-weighted apparent particle size.[65] Measurements carried out over carbon and TiO$_2$ in the absence of Pt exhibited no CO uptake.

The total number of acid sites was determined by NH$_3$ temperature-programmed desorption (NH$_3$-TPD) using an Altamira Instruments AMI-390 system with gas flow rates of 25 mL min^{-1}. Samples of each support (ca. 100 mg) were loaded into a 0.5 in. quartz U-tube reactor and held as a fixed bed between plugs of quartz wool. Oxide samples were pretreated under flowing 10% O$_2$/Ar at 5 K min^{-1} to 773 K and then held at this temperature for 4 h. Carbon samples were pretreated under flowing Ar at 5 K min^{-1} to 773 K and then held at this temperature for 4 h. The samples were cooled to 393 K under flowing He and then saturated with flowing 10% NH$_3$/He for 30 min. Excess and/or physisorbed NH$_3$ was removed by holding the samples at 393 K under flowing He for 1 h. TPD of NH$_3$ was performed by heating the sample from 393 to 773 K at 30 K min^{-1} and then holding for 30 min under flowing He. Desorbed NH$_3$ was measured with a thermal conductivity detector, and calibration was performed after each experiment by introducing 10 pulses of 10% NH$_3$/He from a 5.0 mL sample loop into a stream of flowing He.

Galbraith Laboratories (Knoxville, TN) performed elemental analysis using inductively coupled plasma optical emission spectroscopy (ICP-OES). Samples for TEM were dropcast onto carbon-coated copper grids (Ted Pella part no. 01824) from chloroform or hexanes suspensions. Imaging was performed using a FEI G20 Tecnai operating at 200 keV. The particle size distributions were obtained by the manual measurement of >100 particles using ImageJ software. The average particle diameter was calculated by assuming spherical geometry with no correction for surface wetting. The surface-weighted average particle diameter was calculated using $\sum D_{\mathrm{P,i}}^3/\sum D_{\mathrm{P,i}}^2$ and the volume-weighted average particle diameter was calculated using $\sum D_{\mathrm{P,i}}^4/\sum D_{\mathrm{P,i}}^3$. High-resolution TEM images of Pt/TiO$_2$ were collected at 300 kV using a FEI Tecnai super twin instrument equipped with a thermionic emitter. Samples for high-resolution TEM were dispersed in hexane and distributed on a Si window. Nitrogen physisorption data were collected at 77 K using a Quantachrome Quadrasorb SI instrument. Samples were pretreated under vacuum for 20 h at 473 K. Surface areas were determined using the Brunauer−Emmett−Teller (BET) method with a P/P_0 range of 0.05−0.3.

5.4. Catalytic Testing. Approximately 0.02 g of catalyst was diluted with 177−250 μm diameter particles of silicon carbide to a volume of 4 mL and added to the isothermal zone of a 20 mL downward-flow tubular packed-bed reactor. The temperature of the isothermal zone was monitored using a four-point thermocouple inserted into the catalyst bed. Approximately 2 mL of 150−250 μm diameter crushed quartz was added to each side of the catalyst bed, and the remainder of the reactor was packed with 300−425 μm diameter crushed quartz. To begin an experiment, a gas mixture of hydrogen (95%) and argon (5%) was introduced at the desired WHSV, and the reactor pressure was increased to the desired set point (0.50 or 2.0 MPa). Next, the isothermal zone was heated to the reaction temperature (523 or 623 K) at 5 K min^{-1}. Once the reactor temperature was stable, m-cresol was introduced from an Eldex Optos 1LMP HPLC pump. An 8:1 molar ratio of molecular hydrogen to m-cresol was maintained for the duration of the reaction period, which is twice the stoichiometric requirement for complete hydrogenation to methylcyclohexane and water.

Condensable products from the reaction were collected in a hot trap controlled at 393 K. These products were analyzed using an Agilent Technologies 7890A gas chromatograph equipped with a flame ionization detector and mass spectrometer. Uncondensed products in the gas phase were analyzed online using a separate Agilent Technologies 7890B gas chromatograph modified by Wasson ECE Instrumentation. Products were identified through retention time comparison with known standards and confirmed using mass spectrometry. Quantitative analysis was carried out using flame ionization and thermal conductivity detectors, which had been calibrated with standards of known concentrations. In the event that a standard was unavailable, response factors were extrapolated from similar compounds on the basis of carbon number. Argon was used as an internal standard for the gas-phase analysis, and all values were adjusted to account for changes in total molar flow rate. Gas chromatography was used to determine the molar composition and formula weight of the condensed products. The mass flow rate of the condensed products was determined by dividing the sample mass by the collection time. Using the mass flow rate and formula weight, the total molar flow rate of the condensed phase was calculated. From the total molar flow rate and the molar composition, the individual molar flow rate of each product was determined. In all cases the mass balance closure, based on theoretical inlet flowrates and measured outlet flowrates, was >90%. Both catalysts were highly stable and exhibited <3% change in activity, as determined by guaiacol conversion, during the reaction period. Carbon and TiO$_2$, in the absence of Pt, exhibited no measurable m-cresol conversion during experiments carried out at 623 K. To check for the absence of external and internal mass transfer limitations, the Weisz−Prater and Mears criteria were calculated. The resulting

DOI: 10.1021/acscatal.5b02868
ACS Catal. 2016, 6, 2715−2727

values were significantly below 0.1, indicating that mass transfer limitations did not affect the observed reaction rates.

The conversion of *m*-cresol was calculated according to eq 1 and is defined as the percent decrease in the molar flow rate of *m*-cresol between the feed and outlet of the reactor. The carbon selectivity was calculated according to eq 2 and is defined as the molar flow rate of carbon contained in a product divided by the total molar flow rate of carbon in all products multiplied by 100. The TOF is defined as the molecules of *m*-cresol converted per Pt active site as measured by CO chemisorption.

$$m\text{-cresol conversion} = \left(\frac{[F_{m\text{-cresol}}]_{\text{feed}} - [F_{m\text{-cresol}}]_{\text{outlet}}}{[F_{m\text{-cresol}}]_{\text{feed}}}\right) \times 100 \tag{1}$$

where $F_{m\text{-}cresol}$ = molar flow rate of m-cresol.

$$\text{carbon selectivity} = \left(\frac{F_{\text{C}}}{\sum_{i=1}^{n} F_{\text{C}}}\right) \times 100 \tag{2}$$

where F_i = molar flow rate of carbon in product i and $\sum_{i=1}^{n}(F_i)$ = total molar flow rate of carbon in all products.

5.5. Computational Methods. Calculations were performed using the Vienna Ab initio Simulation Package (VASP) 5.3.[66−69] The periodic density functional calculations used the projector augmented wave (PAW) potentials and an energy cutoff of 400 eV for the plane wave basis set for all calculations.[70,71] The Perdew−Burke−Ernzerhof (PBE)[72] generalized gradient corrected functional was used for all periodic calculations with Monkhorst−Pack 5 × 5 × 1 *k*-point sampling for metals and 3 × 3 × 1 *k*-point sampling for metal oxides. First-order Methfessel−Paxton smearing with $\sigma = 0.2$ eV was used to determine partial occupancies for metallic systems. For TiO_2, a small Gaussian smearing of $\sigma = 0.01$ eV was used to assist in convergence. All reported total energies are extrapolated to zero broadening. As TiO_2 is a strongly correlated material, i.e., one with highly localized electrons, the on-site Coulomb and exchange interactions (Hubbard U correction) were included using the simplified method of Dudarev et al.[73] In this method, only the difference between the on-site values is included. The difference used for these calculations was $U = 2.5$ eV. This value was found to be optimal for barriers and reaction energies for CO reacting on a $TiO_2(101)$ surface by Sorescu et al.[74,75] Optimizations were carried out until the forces were below 0.05 eV/Å for geometry optimizations and below 0.07 eV/Å for nudged elastic band calculations. All optimizations used the quasi-Newton method. The van der Waals (vdW) forces were calculated using the method of Tkatchenko and Scheffler as implemented in VASP.[76,77]

5.6. Computational Models. Slab models were used in the calculations of the Pt(111) and anatase $TiO_2(101)$ surfaces. Pt slab models were formed from the optimized crystal unit cell for platinum. The optimized lattice vectors for the slab were (11.2478, −5.6239, 0.0000 × 0.0000, 9.7409, 0.0000 × 0.0000, 0.0000, 30.0000). The final vector allows for sufficient distance between slabs to avoid unphysical interactions. The surface model is five layers thick with the stoichiometry of Pt_{80}. The upper three layers were relaxed, while the lower layers were fixed at their ideal crystal positions. The $TiO_2(101)$ crystals were optimized by minimizing the energy as a function of volume fit to the Birch−Murnaghan equation of state. After volume optimization, the ratio of the unique lattice vectors c/a was optimized at a constant volume to find the optimal parameters. Energies were calculated, including the Tkatchenko and Scheffler dispersion correction, at U values of 2.5.[76,77] The final values of a = 3.863 Å and c = 9.520 Å were close to the experimental values of a = 3.782 Å and c = 9.502 Å. The optimized lattice vectors in Å for the slab model were (10.2738, 0.0000, 0.0000 × 0.0000, 11.5904, 0.0000 × 0.0000, 0.0000, 33.5747).

Previous work using ab initio thermodynamics and DFT indicate that the Pt(111) surface would exhibit significant hydrogen coverage at the experimental temperatures and pressures used in this study.[59,60,78−80] While the surface is likely to contain a significant amount of adsorbed aromatic species, this high-coverage effect may be modeled primarily by coverage of a simple adsorbate such as hydrogen.[81] For these reasons, all of the calculations were started using a surface with a complete hydrogen monolayer or a single surface vacancy in the hydrogen monolayer, as shown in Figure 11 at the atop sites.[82] All Pt(111) models used in these calculations were started with hydrogen atoms at atop sites.

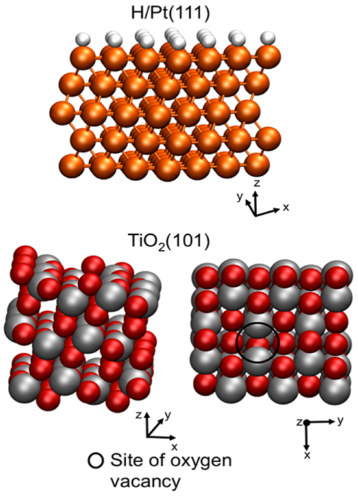

Figure 11. Hydrogen-covered Pt(111) and anatase $TiO_2(101)$ models (side and top-down views) used in this study. The small white spheres represent hydrogen atoms, the orange spheres platinum atoms, the silver spheres titanium atoms, and the red spheres oxygen atoms.

The most common defect in the $TiO_2(101)$ surface is an oxygen vacancy.[55,83] These vacancies create undercoordinated sites that are the most likely source of reactivity with oxygenated aromatics.[44] Oxygen vacancies in the $TiO_2(101)$ lattice were formed by removing a two-coordinate oxygen atom from the surface, as illustrated in Figure 11. This vacancy was previously found to have the lowest formation energy.[55,83] The energies were determined relative to the reactant in all cases. Barriers were determined using nudged elastic band calculations with 7−11 images between the reactants and products. Potential energy surfaces (PES) were made from combining calculations of elementary steps. The energies were corrected for intermediates by adding corrections to ensure each step had the same number and type of atoms as well as the same number of electrons. In most instances, the difference for the energy of a structure calculated using corrected and uncorrected references was below 0.05 eV. Cases where this was not true correspond to differences in molecular configuration only.

DOI: 10.1021/acscatal.5b02868
ACS Catal. 2016, 6, 2715−2727

■ ASSOCIATED CONTENT

Ⓢ Supporting Information

The Supporting Information is available free of charge on the ACS Publications website at DOI: 10.1021/acscatal.5b02868.

> XRD patterns of carbon and Pt/C, micrograph of Pt/TiO_2, NH_3-TPD profiles of carbon and TiO_2, time on stream reaction data for Pt/TiO_2 and Pt/C, and detailed steps in the reaction pathways for *m*-cresol deoxygenation over the TiO_2(101) and Pt(111) surfaces, including energy profiles and important bond lengths and distances (PDF)

■ AUTHOR INFORMATION

Corresponding Authors

*E-mail for G.T.B.: gregg.beckham@nrel.gov.

*E-mail for J.A.S.: joshua.schaidle@nrel.gov.

Author Contributions

[†]These author contributed equally.

Notes

The authors declare no competing financial interest.

■ ACKNOWLEDGMENTS

This work was supported by the U.S. Department of Energy's Bioenergy Technologies Office, Contract No. DE-AC36-08GO28308, at the National Renewable Energy Laboratory. Computer time was provided by the Texas Advanced Computing Center under the National Science Foundation Extreme Science and Engineering Discovery Environment Grant MCB-090159 and by the National Renewable Energy Laboratory Computational Sciences Center. The authors thank NREL researchers Mayank Behl (chemisorption measurements), Matt Yung (chemisorption measurements), Susan Habas (TEM imaging), Jeffery Aguiar (TEM imaging), and Erick White (reactor operation). Helpful discussions with Samuel Dull, Connor Nash, and Vassili Vorotnikov are also gratefully acknowledged. The U.S. Government retains and the publisher, by accepting the article for publication, acknowledges that the U.S. Government retains a nonexclusive, paid up, irrevocable, worldwide license to publish or reproduce the published form of this work, or allow others to do so, for U.S. Government purposes.

■ REFERENCES

(1) Czernik, S.; Bridgwater, A. V. *Energy Fuels* **2004**, *18*, 590−598.

(2) Yaman, S. *Energy Convers. Manage.* **2004**, *45*, 651−671.

(3) Mortensen, P. M.; Grunwaldt, J. D.; Jensen, P. A.; Knudsen, K. G.; Jensen, A. D. *Appl. Catal., A* **2011**, *407*, 1−19.

(4) Kersten, S.; Swaaij, W. v.; Lefferts, L.; Seshan, K. *Catalysis for Renewables: From Feedstock to Energy Production*; Centi, G., van Santen, R. A., Eds.; Wiley-VCH: Weinheim, Germany, 2007; pp 119−145.

(5) Bridgwater, A. V. *Environ. Prog. Sustainable Energy* **2012**, *31*, 261−268.

(6) Ruddy, D. A.; Schaidle, J. A.; Ferrell, J. R., III; Wang, J.; Moens, L.; Hensley, J. E. *Green Chem.* **2014**, *16*, 454−490.

(7) Dutta, A.; Schaidle, J.; Humbird, D.; Baddour, F.; Sahir, A. *Top. Catal.* **2016**, *59*, 2−18.

(8) Venkatakrishnan, V. K.; Delgass, W. N.; Ribeiro, F. H.; Agrawal, R. *Green Chem.* **2015**, *17*, 178−183.

(9) Talmadge, M. S.; Baldwin, R. M.; Biddy, M. J.; McCormick, R. L.; Beckham, G. T.; Ferguson, G. A.; Czernik, S.; Magrini-Bair, K. A.; Foust, T. D.; Metelski, P. D.; Hetrick, C.; Nimlos, M. R. *Green Chem.* **2014**, *16*, 407−453.

(10) de Souza, P. M.; Rabelo-Neto, R. C.; Borges, L. E. P.; Jacobs, G.; Davis, B. H.; Sooknoi, T.; Resasco, D. E.; Noronha, F. B. *ACS Catal.* **2015**, *5*, 1318−1329.

(11) Nie, L.; Resasco, D. E. *J. Catal.* **2014**, *317*, 22−29.

(12) Lu, J. M.; Behtash, S.; Mamun, O.; Heyden, A. *ACS Catal.* **2015**, *5*, 2423−2435.

(13) Gutierrez, A.; Kaila, R. K.; Honkela, M. L.; Slioor, R.; Krause, A. O. I. *Catal. Today* **2009**, *147*, 239−246.

(14) Runnebaum, R. C.; Nimmanwudipong, T.; Block, D. E.; Gates, B. C. *Catal. Lett.* **2011**, *141*, 817−820.

(15) Nimmanwudipong, T.; Aydin, C.; Lu, J.; Runnebaum, R. C.; Brodwater, K. C.; Browning, N. D.; Block, D. E.; Gates, B. C. *Catal. Lett.* **2012**, *142*, 1190−1196.

(16) Nimmanwudipong, T.; Runnebaum, R. C.; Block, D. E.; Gates, B. C. *Energy Fuels* **2011**, *25*, 3417−3427.

(17) Boonyasuwat, S.; Omotoso, T.; Resasco, D. E.; Crossley, S. P. *Catal. Lett.* **2013**, *143*, 783−791.

(18) Elliott, D. C.; Hart, T. R. *Energy Fuels* **2009**, *23*, 631−637.

(19) Nimmanwudipong, T.; Runnebaum, R. C.; Block, D. E.; Gates, B. C. *Catal. Lett.* **2011**, *141*, 779−783.

(20) Tan, Q.; Wang, G.; Nie, L.; Dinse, A.; Buda, C.; Shabaker, J.; Resasco, D. E. *ACS Catal.* **2015**, *5*, 6271−6283.

(21) Griffin, M.; Baddour, F.; Habas, S.; Ruddy, D.; Schaidle, J. *Top. Catal.* **2016**, *59*, 124−137.

(22) Furimsky, E. *Appl. Catal., A* **2000**, *199*, 147−190.

(23) Foster, A. J.; Do, P. T. M.; Lobo, R. F. *Top. Catal.* **2012**, *55*, 118−128.

(24) Gao, D.; Schweitzer, C.; Hwang, H. T.; Varma, A. *Ind. Eng. Chem. Res.* **2014**, *53*, 18658−18667.

(25) Saidi, M.; Samimi, F.; Karimipourfard, D.; Nimmanwudipong, T.; Gates, B. C.; Rahimpour, M. R. *Energy Environ. Sci.* **2014**, *7*, 103−129.

(26) Nie, L.; de Souza, P. M.; Noronha, F. B.; An, W.; Sooknoi, T.; Resasco, D. E. *J. Mol. Catal. A: Chem.* **2014**, *388-389*, 47−55.

(27) Li, Y.; Xu, X.; Zhang, P.; Gong, Y.; Li, H.; Wang, Y. *RSC Adv.* **2013**, *3*, 10973−10982.

(28) Zhu, X.; Nie, L.; Lobban, L. L.; Mallinson, R. G.; Resasco, D. E. *Energy Fuels* **2014**, *28*, 4104−4111.

(29) Massoth, F. E.; Politzer, P.; Concha, M. C.; Murray, J. S.; Jakowski, J.; Simons, J. *J. Phys. Chem. B* **2006**, *110*, 14283−14291.

(30) Runnebaum, R. C.; Lobo-Lapidus, R. J.; Nimmanwudipong, T.; Block, D. E.; Gates, B. C. *Energy Fuels* **2011**, *25*, 4776−4785.

(31) Nimmanwudipong, T.; Runnebaum, R. C.; Ebeler, S. E.; Block, D. E.; Gates, B. C. *Catal. Lett.* **2012**, *142*, 151−160.

(32) Li, K.; Wang, R.; Chen, J. *Energy Fuels* **2011**, *25*, 854−863.

(33) Runnebaum, R. C.; Nimmanwudipong, T.; Block, D. E.; Gates, B. C. *Catal. Sci. Technol.* **2012**, *2*, 113−118.

(34) Lee, K.; Gu, G. H.; Mullen, C. A.; Boateng, A. A.; Vlachos, D. G. *ChemSusChem* **2015**, *8*, 315−322.

(35) Chiu, C.-c.; Genest, A.; Borgna, A.; Roesch, N. *ACS Catal.* **2014**, *4*, 4178−4188.

(36) Chiu, C.-c.; Genest, A.; Borgna, A.; Roesch, N. *Phys. Chem. Chem. Phys.* **2015**, *17*, 15324−15330.

(37) Ghampson, I. T.; Sepulveda, C.; Garcia, R.; Fierro, J. L.; Escalona, N.; DeSisto, W. J. *Appl. Catal., A* **2012**, *435-436*, 51−60.

(38) Omotoso, T.; Boonyasuwat, S.; Crossley, S. P. *Green Chem.* **2014**, *16*, 645−652.

(39) Chang, J.; Danuthai, T.; Dewiyanti, S.; Wang, C.; Borgna, A. *ChemCatChem* **2013**, *5*, 3041−3049.

(40) Corpuz, A. R.; Pang, S. H.; Schoenbaum, C. A.; Medlin, J. W. *Langmuir* **2014**, *30*, 14104−14110.

(41) Nakagawa, Y.; Nakazawa, H.; Watanabe, H.; Tomishige, K. *ChemCatChem* **2012**, *4*, 1791−1797.

(42) Wan, H.; Chaudhari, R. V.; Subramaniam, B. *Top. Catal.* **2012**, *55*, 129−139.

(43) Zhao, H. Y.; Li, D.; Bui, P.; Oyama, S. T. *Appl. Catal., A* **2011**, *391*, 305−310.

(44) Schimming, S. M.; LaMont, O. D.; Koenig, M.; Rogers, A. K.; D'Amico, A. D.; Yung, M. M.; Sievers, C. *ChemSusChem* **2015**, *8*, 2073−2083.
(45) de Souza, P. M.; Nie, L.; Borges, L. E. P.; Noronha, F. B.; Resasco, D. E. *Catal. Lett.* **2014**, *144*, 2005−2011.
(46) Hensley, A. J. R.; Wang, Y.; McEwen, J.-S. *ACS Catal.* **2015**, *5*, 523−536.
(47) Sun, J.; Karim, A. M.; Zhang, H.; Kovarik, L.; Li, X. S.; Hensley, A. J.; McEwen, J.-S.; Wang, Y. *J. Catal.* **2013**, *306*, 47−57.
(48) Zhao, C.; He, J.; Lemonidou, A. A.; Li, X.; Lercher, J. A. *J. Catal.* **2011**, *280*, 8−16.
(49) Do, P. T. M.; Foster, A. J.; Chen, J.; Lobo, R. F. *Green Chem.* **2012**, *14*, 1388−1397.
(50) Zhu, X.; Lobban, L. L.; Mallinson, R. G.; Resasco, D. E. *J. Catal.* **2011**, *281*, 21−29.
(51) Krupski, K.; Moors, M.; Jóźwik, P.; Kobiela, T.; Krupski, A. *Materials* **2015**, *8*, 2935.
(52) Shao, M. H.; Peles, A.; Shoemaker, K. *Nano Lett.* **2011**, *11*, 3714−3719.
(53) Schweitzer, N. M.; Schaidle, J. A.; Ezekoye, O. K.; Pan, X.; Linic, S.; Thompson, L. T. *J. Am. Chem. Soc.* **2011**, *133*, 2378−2381.
(54) Lam, E.; Luong, J. H. T. *ACS Catal.* **2014**, *4*, 3393−3410.
(55) Conradie, J.; Gracia, J.; Niemantsverdriet, J. W. *J. Phys. Chem. C* **2012**, *116*, 25362−25367.
(56) Prins, R. *Chem. Rev.* **2012**, *112*, 2714−2738.
(57) Badawi, M.; Paul, J. F.; Payen, E.; Romero, Y.; Richard, F.; Brunet, S.; Popov, A.; Kondratieva, E.; Gilson, J. P.; Mariey, L.; Travert, A.; Mauge, F. *Oil Gas Sci. Technol.* **2013**, *68*, 829−840.
(58) Bui, V. N.; Toussaint, G.; Laurenti, D.; Mirodatos, C.; Geantet, C. *Catal. Today* **2009**, *143*, 172−178.
(59) Chizallet, C.; Bonnard, G.; Krebs, E.; Bisson, L.; Thomazeau, C.; Raybaud, P. *J. Phys. Chem. C* **2011**, *115*, 12135−12149.
(60) Chizallet, C.; Digne, M.; Arrouvel, C.; Raybaud, P.; Delbecq, F.; Costentin, G.; Che, M.; Sautet, P.; Toulhoat, H. *Top. Catal.* **2009**, *52*, 1005−1016.
(61) Li, G.; Han, J.; Wang, H.; Zhu, X.; Ge, Q. *ACS Catal.* **2015**, *5*, 2009−2016.
(62) Nelson, R. C.; Baek, B.; Ruiz, P.; Goundie, B.; Brooks, A.; Wheeler, M. C.; Frederick, B. G.; Grabow, L. C.; Austin, R. N. *ACS Catal.* **2015**, *5*, 6509−6523.
(63) Romanmartinez, M. C.; Cazorlaamoros, D.; Linaressolano, A.; Delecea, C. S. *Carbon* **1993**, *31*, 895−902.
(64) Ebitani, K.; Hattori, H. *Bull. Chem. Soc. Jpn.* **1991**, *64*, 2422−2427.
(65) Karakaya, C.; Deutschmann, O. *Appl. Catal., A* **2012**, *445-446*, 221−230.
(66) Kresse, G.; Furthmuller, J. *Phys. Rev. B: Condens. Matter Mater. Phys.* **1996**, *54*, 11169−11186.
(67) Kresse, G.; Furthmuller, J. *Comput. Mater. Sci.* **1996**, *6*, 15−50.
(68) Kresse, G.; Hafner, J. *Phys. Rev. B: Condens. Matter Mater. Phys.* **1993**, *47*, 558−561.
(69) Kresse, G.; Hafner, J. *Phys. Rev. B: Condens. Matter Mater. Phys.* **1994**, *49*, 14251−14269.
(70) Blochl, P. E. *Phys. Rev. B: Condens. Matter Mater. Phys.* **1994**, *50*, 17953−17979.
(71) Kresse, G.; Joubert, D. *Phys. Rev. B: Condens. Matter Mater. Phys.* **1999**, *59*, 1758−1775.
(72) Perdew, J. P.; Burke, K.; Ernzerhof, M. *Phys. Rev. Lett.* **1996**, *77*, 3865−3868.
(73) Dudarev, S. L.; Botton, G. A.; Savrasov, S. Y.; Humphreys, C. J.; Sutton, A. P. *Phys. Rev. B: Condens. Matter Mater. Phys.* **1998**, *57*, 1505−1509.
(74) Sorescu, D. C.; Al-Saidi, W. A.; Jordan, K. D. *J. Chem. Phys.* **2011**, *135*, 124701.
(75) Sorescu, D. C.; Civis, S.; Jordan, K. D. *J. Phys. Chem. C* **2014**, *118*, 1628−1639.
(76) Tkatchenko, A.; DiStasio, R. A.; Car, R.; Scheffler, M. *Phys. Rev. Lett.* **2012**, *108*, 236402.
(77) Tkatchenko, A.; Scheffler, M. *Phys. Rev. Lett.* **2009**, *102*, 073005.
(78) Jin, H.; Wang, L.; Searles, D. J.; Sun, C. *Chin. Sci. Bull.* **2014**, *59*, 2175−2180.
(79) Neurock, M.; Pallassana, V.; van Santen, R. A. *J. Am. Chem. Soc.* **2000**, *122*, 1150−1153.
(80) Wang, S.; Vorotnikov, V.; Vlachos, D. G. *ACS Catal.* **2015**, *5*, 104−112.
(81) Burkholder, L.; Stacchiola, D.; Tysoe, W. *Surf. Rev. Lett.* **2003**, *10*, 909−916.
(82) Saeys, M.; Reyniers, M. F.; Neurock, M.; Marin, G. B. *J. Phys. Chem. B* **2005**, *109*, 2064−2073.
(83) Vittadini, A.; Casarin, M.; Selloni, A. *Theor. Chem. Acc.* **2007**, *117*, 663−671.

DOI: 10.1021/acscatal.5b02868
ACS Catal. 2016, 6, 2715−2727